Decreasing seasonal cycle amplitude of methane in the northern high latitudes being driven by lower latitude changes in emissions and transport

Emily Dowd[1], Chris Wilson[1,2], Martyn P. Chipperfield[1,2], Emanuel Gloor[3], Alistair Manning[4], and Ruth Doherty[5]

[1]School of Earth & Environment, University of Leeds, Leeds, UK
[2]National Centre for Earth Observation, University of Leeds, Leeds, UK
[3]School of Geography, University of Leeds, Leeds, UK
[4]Met Office, Exeter, UK
[5]School of GeoSciences, University of Edinburgh, Edinburgh, UK

Correspondence: Emily Dowd (eeed@leeds.ac.uk)

Abstract. Atmospheric methane (CH_4) concentrations are rising which is expected to lead to a corresponding increase in its global seasonal cycle amplitude (SCA), the difference between its seasonal maximum and minimum values. Spatially-varying changes in the SCA could indicate long-term persistent variations in the seasonal sources and sinks but such SCA changes have not been investigated. Here we use surface flask measurements and a 3-D chemical transport model (TOMCAT) to diagnose changes in the SCA of atmospheric CH_4 between 1995-2020 and attribute the changes regionally to contributions from different sectors. We find that the observed SCA decreased by 4 ppb (7.6%) in the northern high latitudes (NHL, 60°N-90°N), whilst globally the SCA increased by 2.5 ppb (6.5%) during this time period. TOMCAT reproduces the change in the SCA at observation sites across the globe and therefore we use it to attribute regions which are contributing to the changes in the NHL SCA. We find that well-mixed background CH_4, likely from emissions originating in, and transported from, more southerly latitudes has the largest impact on the decreasing SCA in the NHL (56.5% of total contribution to NHL). In addition to the background CH_4, recent emissions from Canada, the Middle East and Europe contribute 16.9%, 12.1% and 8.4%, respectively, to the total change in the SCA in the NHL. The regional contributions are driven by increases in summer emissions from the Boreal Plains in Canada, decreases in winter emissions across Europe, and a combination of increases in summer emissions and decreases in winter emissions over the Arabian Peninsula and Caspian Sea in the Middle East. These results highlight that changes in the observed seasonal cycle can be an indicator of changing emission regimes in local and non-local regions, particularly in the NHL where the change is counter-intuitive.

1 Introduction

Methane (CH$_4$) is the second most important anthropogenic greenhouse gas in the atmosphere after carbon dioxide (CO$_2$)
20 and anthropogenic emissions have contributed an extra 23% to the radiative forcing in the troposphere since 1750 (Saunois
et al., 2020). Global observations by the National Oceanic and Atmospheric Administration (NOAA) Earth System Research
Laboratories (ESRL) show that concentrations of atmospheric CH$_4$ have risen since the 1980s, with a short hiatus in the
growth between 1999 and 2006. Our understanding of the drivers of the global trends of CH$_4$ remains incomplete (Nisbet
et al., 2016, 2019; Dlugokencky et al., 2021). Long-term trends of CH$_4$ are monitored through surface flask observations by
25 NOAA ESRL and have been studied extensively. Long-term variations in the seasonal cycle of CH$_4$ have not been analysed
in detail since a study by Dlugokencky et al. (1997), although several studies have briefly discussed its seasonal cycle (e.g.
Pickett-Heaps et al. (2011); Bergamaschi et al. (2018); Patra et al. (2011); Parker et al. (2020)).

CH$_4$ has a mixture of natural and anthropogenic sources and chemical sinks which lead to a strong seasonal cycle in the
atmosphere. Figure 1 shows the mean seasonal cycle across NOAA observation sites (Table 1) in the northern and southern
30 hemispheres, where concentrations are at a minimum in summer and peak in winter or early spring, depending on location.
The atmospheric CH$_4$ seasonal cycle is driven by the seasonal variations of sources such as wetlands, rice paddies and biomass
burning, the chemical loss of CH$_4$ in the atmosphere, and the transport of CH$_4$. The main sources which drive the CH$_4$ cycle
are dependent on climatological and meteorological conditions. Emissions from wetlands and rice paddies vary seasonally
with changes in temperature, precipitation and soil moisture. Biomass burning emissions in the tropics and boreal regions
35 also vary seasonally (Dlugokencky et al., 1997). It is thought that anthropogenic emissions play a smaller role in the seasonal
cycle of CH$_4$ (e.g. Meirink et al. (2008); Wilson et al. (2021)) but few studies have investigated the long-term influence of
anthropogenic emissions on the observed seasonal cycle. For example, anthropogenic emissions might increase in winter due
to increased gas extraction (Nisbet et al., 2019). The sinks of CH$_4$ also play a large role in the seasonal cycle. The main sink
of CH$_4$ is the hydroxyl radical (OH) which is photochemically produced, which results in the local abundance of OH varying
40 seasonally due to the availability of UV radiation. Finally, transport of CH$_4$ in the atmosphere through advection, convection
and global circulation transporting air to the poles also influences the seasonal cycle.

Many studies have assessed how well wetland models and chemical transport models reproduce the observed CH$_4$ seasonal
cycle, the timing of the seasonal maximum and seasonal minimum, or what might be driving the seasonal cycle on a regional
scale (Patra et al., 2011; Bergamaschi et al., 2018; Parker et al., 2020). These studies did not explore how the seasonal cycle
45 amplitude (SCA) has changed over time on a global scale. The SCA is defined as the difference between the annual maximum
and the annual minimum concentration at a particular location. Changes in the seasonality of emissions will be reflected in
the seasonal cycle amplitude of CH$_4$ and will ultimately impact the annual growth rate. However, changes in loss rates and
transport add extra complexity to assessing changes in the seasonal cycle. Studying the SCA could give us a better insight
into changes in the CH$_4$ budget. In this study we regionally attribute the change in SCA of CH$_4$ between 1995-2020 using the
50 TOMCAT chemical transport model (Chipperfield, 2006) and surface observations from NOAA ESRL (Dlugokencky et al.,
2021).
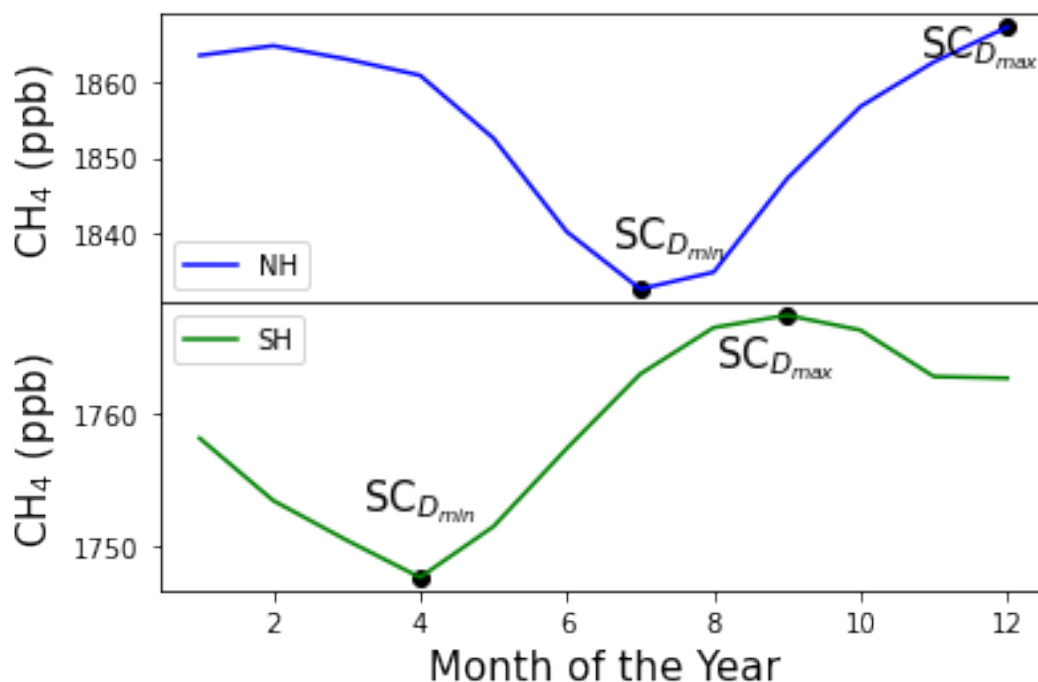
Figure 1. The monthly mean CH_4 mixing ratio (ppb) across northern hemisphere (NH) and southern hemisphere (SH) at 22 NOAA surface sites between 1995-2022 (see Table 1). $SC_{D_{max}}$ and $SC_{D_{min}}$ represent the seasonal cycle maximum and minimum, respectively.

In Sect. 2 we describe the observations used, the modelling methodology and the SCA analysis. In Sect. 3 and Sect. 4 we present our results and discuss our findings.

2 Methods

2.1 Atmospheric Methane Measurements

We assimilate and analyse the long-term surface flask measurements provided by NOAA ESRL. The air samples are collected approximately weekly or biweekly and CH_4 is measured using gas chromatography with flame ionization detection or by cavity ring-down spectroscopy methods (Dlugokencky et al., 2021). The NOAA observation network provides measurements across the globe, but there is a disproportionate number of sites in the northern hemisphere compared with the southern hemisphere, see Fig. 2. There is also a lack of regular observations in some tropical regions, where there are large and uncertain CH_4 emissions.

We assimilate NOAA surface observations in INVICAT, the inverse model of TOMCAT, in order to get optimised estimates of CH_4 fluxes to use in the TOMCAT forward model. We used observations from 80 NOAA surface observation sites and assimilated them at the correct model time step. Full details of the assimilation can be found in Sect. 2.3. In the SCA analysis

65 we used a subset of these observations. We calculated the monthly mean CH$_4$ at 22 NOAA surface sites which were selected
if they contained observations for the entire period 1995-2020 and were not strongly influenced by local sources (McNorton
et al., 2018). A list of the sites and their site codes are in Table 1 and their locations are shown by the blue dots in Fig. 2. We also
evaluate the model performance using observations from the Center for Global Environmental Research Earth System Division,
National Institute for Environmental Studies, Japan (NIES, Tohjima et al. (2002); Sasakawa et al. (2010)) and the Advanced

70 Global Atmospheric Gases Experiment (AGAGE, Prinn et al. (2018)) which have not been assimilated, see Supplement Fig.
S1. The sites from NIES are in Siberia and East Asia and the site from AGAGE is situated in Ireland, their locations are shown
as the red dots in Fig. 2. The independent observations do not cover the whole study period but we have maximised the time
period available from each data set by selecting a period with the most regular observations. The NIES observations in Siberia
are from 2009-2015, the remaining NIES observations are from 1997-2015 and the AGAGE observations are from 1996-2020.

75 ## 2.2 Tagged Transport Simulations

TOMCAT is a three-dimensional (3D) atmospheric chemical transport model which has been used in a number of studies to
model CH$_4$ and other chemical species in the atmosphere (e.g. Chipperfield (2006); Parker et al. (2018); Wilson et al. (2021)).
We use TOMCAT to investigate changes in the SCA of CH$_4$ between 1995 and 2020, including the impact of changes in
emissions and transport. The globe was divided into 18 different regions, shown in Fig. 2, in order to attribute the changes in

80 the SCA from particular regions. The regions were selected based on the magnitude and type of emission in the distribution used
in TOMCAT. The northern oceans, Greenland, Iceland and Svalbard have been grouped together (North Oceans and Arctic,
NOA), as were the southern oceans and Antarctica (SOA). Northern land regions have been split into Canada (CAN), Europe
(EUR) and Russia (RUS) due to their emissions types and geographical location. The emissions from these regions include
anthropogenic emissions such as those from oil and gas industries, livestock and other agriculture, but also include natural

85 emissions such as those from wetlands and biomass burning. In the northern mid-latitudes regions such as North America
(NAM), Middle East (ME) and China & Japan (CHJA) are dominated by large anthropogenic emissions. Africa has been split
into three regions because of the influence of central Africa in the CH$_4$ budget, with recent studies highlighting the large role
tropical wetlands play in the recent global growth (Lunt et al., 2021; Feng et al., 2022). Similarly, Brazil has been split into
three regions due to the local emission sectors and different responses to seasonal changes in meteorology (Wilson et al., 2021;

90 Basso et al., 2021). The North Brazil (NBRA) emissions are mostly driven by wetlands, whereas East Brazil (EBRA) is more
susceptible to biomass burning in the arc of deforestation, a region of regular and intense anthropogenic burning. The South
Brazil (SBRA) emissions are driven by a mixture of both wetlands and biomass burning. The rest of South America has been
grouped as Non-Amazon South America. Emissions from the South East Asia region (SEA) is from a mixture of rice paddies,
biomass burning and other anthropogenic emissions, whilst Australia (AUS) is mostly driven by anthropogenic emissions, such

95 as those from coal mines. The names given to each region are given in Table 2.

Emissions from each region were simulated separately in the model and could be summed to represent global CH$_4$. This is
possible due to the linearity of the TOMCAT model transport (Wilson et al., 2016) and offline (non-interactive) loss rates. In
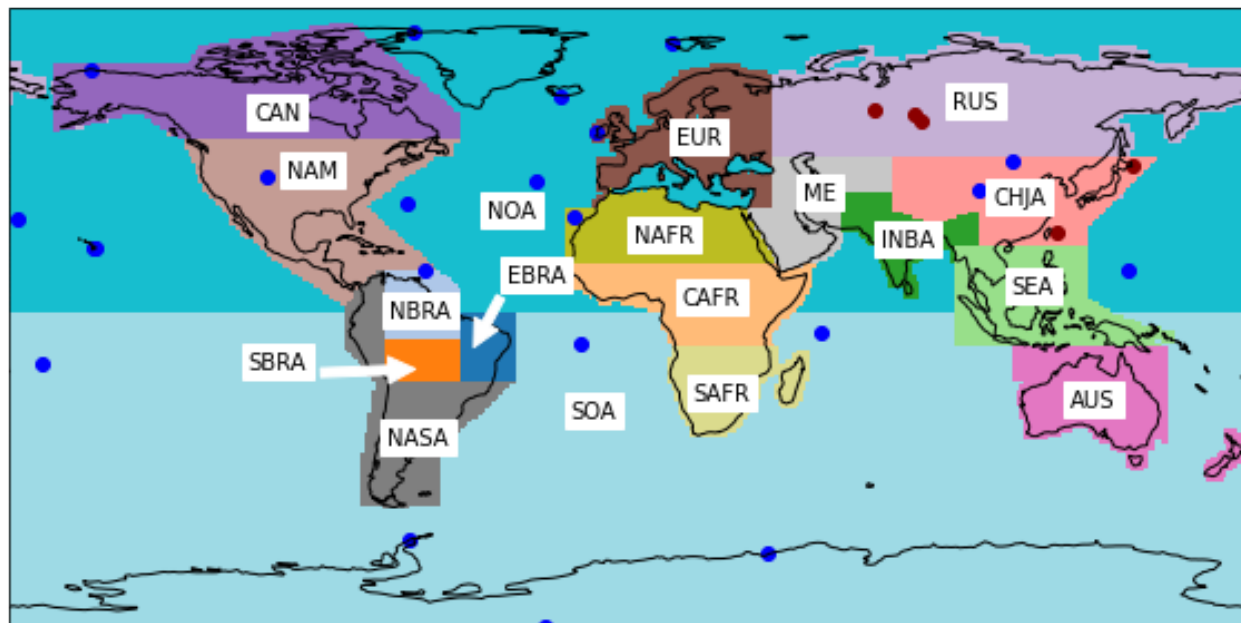
Figure 2. A map showing the 18 different regions selected for the tagged tracers, 22 NOAA surface observation site locations (blue) and the independent observations site locations (red).

reality, the loss of CH_4 is not linear because the abundance of CH_4 impacts its rate of loss due to its impact on OH abundance, but this is a small effect relative to the large CH_4 abundance.

100   TOMCAT was run at a $5.6° \times 5.6°$ horizontal resolution with 60 vertical levels up to 0.1 hPa, between 1983 and 2020 for each regional tagged tracer, a background tracer and a total CH_4 tracer. The background tracer contains CH_4 from the regional tracers once the CH_4 from each region has become well-mixed. Each regional tagged tracer was set to be reallocated into the background tracer using an exponential 9-month decay rate. The 9-month decay rate was selected in order to maximise the opportunity for CH_4 to undergo long-range transport from emission locations to surface sites, whilst minimising the effect of

105 well-mixed atmospheric CH_4 on the results. The study period begins in 1995 to allow the tracers to become well-mixed in the preceding 12 years. This model simulation is called TOM_regional and uses surface fluxes derived from a TOMCAT-based atmospheric inversion described in Sect. 2.3. The meteorology was driven by the European Centre for Medium-Range Weather Forecasts (ECMWF) ERA5 reanalyses (Hersbach et al., 2020) and the OH fields for the troposphere and stratosphere were based on those within the TransCom CH_4 study (Patra et al., 2011). The OH fields were originally taken from Spivakovsky

110 et al. (2000) and scaled downwards by 8% in accordance with Huijnen et al. (2010) in order to match the observed methyl chloroform concentrations in the atmosphere (Patra et al., 2011). The stratospheric loss rates for Cl and $O(^1D)$ varied annually and were taken from a previous full chemistry TOMCAT simulation (Monks et al., 2017). The soil sink was taken from the

MeMo model which varied each year between 1990 to 2009, the 1990 values were annually repeated from 1983-1990 and similarly, the 2009 values were repeated annually from 2009-2020 (Murguia-Flores et al., 2018).

115   We carried out two sensitivity experiments to investigate the impact of the choice of the exponential lifetime used to allocate well-mixed CH_4 into the background tracer, and if it influences the background tracer's contribution to the change in the SCA. Decay rates of 1 and 12 months were selected to show the impact of a short and long decay timescales on the background and regional contributions of the change in the SCA. The simulations are labelled TOM_one for the 1-month decay rate and TOM_twelve for the 12-month rate. The results of the sensitivity experiments can be found in Sect. 3.5.

120   The TOM_regional simulation quantifies the impact regional emissions have on the SCA of CH_4 elsewhere under annually varying transport processes. In order to investigate the role that those transport processes alone play in the change in SCA of CH_4, we also carried out a separate regional tagged tracer simulation using annually-repeating emissions for the same time period. Using annually-repeating values removes the influence of changing emissions, allowing us to investigate changes to the transport undergone by emissions from each region over time. The surface emissions for each month of the year were averaged

125 between 1983-2020. These emissions were repeated annually using the same model set-up as TOM_regional and the same analysis of SCA was repeated for 1995-2020. This constant emissions simulation is labelled TOM_transport. A summary of the TOMCAT simulations can be found in Table 3.

2.3   Fluxes from Atmospheric Inversions

The surface fluxes for the tagged tracer simulations were derived using the TOMCAT-based inverse model, INVICAT (Wilson

130 et al., 2014). INVICAT has been used in a number of studies to constrain emissions of various species, including CH_4 (Gloor et al., 2018; Wilson et al., 2021). It uses a 4D-Var variational method based on that used in Numerical Weather Prediction, with full details on the methods used in INVICAT given in Wilson et al. (2014). The inverse method aims to minimise the value of a cost function, in a least-squares sense. The cost function combines an error-weighted sum of the differences between the model and observations and the uncertainty-weighted sum of changes to the a priori flux estimate (Wilson et al., 2021). The input

135 for INVICAT includes an a priori mean flux value for each grid cell and an error covariance matrix containing the covariances between the flux uncertainties. The output is an a posteriori mean grid cell flux and error covariance matrix. The a priori and a posteriori fluxes will hence be referred to as prior fluxes and posterior fluxes, respectively.

    The inverse model simulations were run at a $5.6° \times 5.6°$ horizontal resolution with 60 vertical levels up to 0.1 hPa and a time step of 30 min. The meteorology was taken from ECMWF's ERA5 reanalyses (Hersbach et al., 2020). An inversion was carried

140 out separately for each year and completed 40 minimisation iterations. The 40 iterations were sufficient for the cost function and its gradient norm to be judged as converged, based on both being smaller than 1% of their initial value. The inversion for each year was run for 14 months, until February the following year, in order to better constrain the fluxes in the final months of each year. The final 2 months of each are discarded from the results. Each inversion overlapped with the following one by 2 months but they were initialised using 3-D fields provided from the correct date in the previous year so the total CH_4 burden

145 was conserved across each year.

The 4D-Var-simulated CH_4 mixing ratios were linearly interpolated to the correct longitude, latitude and altitude of each surface observation used in the inversion at the nearest model time step. The surface observations were given uncorrelated errors of 3 ppb plus a representation error. The representation error was estimated as the mean difference across eight grid cells around the cell which contained the observation. The prior emissions were taken from various inventories. The anthropogenic emissions were taken from EDGARv5 (Crippa et al., 2021), excluding rice paddies and fires. The biomass burning emissions were taken from GFEDv4.1s (Randerson et al., 2017). The WetCHARTS model (Bloom et al., 2017) in a median set-up was used for the wetland fluxes. The median set-up uses the median scaling factor and temperature response from the WetCHARTS suite and the Global Lakes and Wetlands Database distribution of wetlands. The wetland fluxes were then masked to remove emissions which overlap with rice emissions and then scaled back up to 180 Tg to match the mean value from the Global Methane Budget (Saunois et al., 2020). The rice and termite emissions were taken from the Transcom intercomparison project (Patra et al., 2011). The termite emissions were scaled to match the total quoted in Saunois et al. (2020). The geological emissions were from Etiope et al. (2019) and the ocean emissions are taken from Weber et al. (2019). The prior emissions are given cell uncertainties of 250% of the prior flux value but also include 500 km spatial correlations with a Gaussian distribution for all fluxes. Fossil fuel fluxes have temporal correlations based on an exponential distribution with a time scale of 9 months. The tropospheric and stratospheric loss rates are the same as those used in the TOMCAT tagged tracer simulations (Sect. 2.2).

2.4 Data Processing and Analysis

The monthly mean model output from TOMCAT was interpolated horizontally and vertically to the 22 surface observation sites (Table 1) from NOAA's ESRL (Dlugokencky et al., 2021) to check model performance and in order to investigate the regional contribution to the change in SCA at these sites. Following methods used by Lin et al. (2020) for CO_2, the seasonal cycle amplitude (SCA) of CH_4 and the regional contribution to the SCA was analysed.

To calculate the SCA, we isolate the mean annual cycle observed in CH_4 by taking the interpolated model output at each surface observation site and then smooth and detrend the time series using the CCGCRV curve-fitting routine, developed by Thoning et al. (1989). CCGCRV approximates the seasonal cycle and long-term trend variation by fitting a polynomial equation combined with a harmonic function (Pickers and Manning, 2015). The short-term and long-term cut off values can be selected and we chose 80-day and 667-day cut offs, respectively Dlugokencky et al. (1994). These parameters have been used in previous studies (Dlugokencky et al., 1994; Parker et al., 2018). The SCA for the observations and the modelled total tracer was calculated by taking the difference between the annual maximum (SC_{Dmax}) and annual minimum (SC_{Dmin}) of the detrended curve:

$$SCA = SC_{Dmax} - SC_{Dmin} \tag{1}$$

where D_{max} and D_{min} are the days of the annual CH_4 cycle maximum and minimum. For each tagged regional tracer, i, a pseudo SCA (SCA') was calculated where the pseudo maximum ($SC'_{i,D_{max}}$) or minimum ($SC'_{i,D_{min}}$) is the point of its annual cycle corresponding to D_{max} and D_{min}. The pseudo seasonal cycle amplitude was calculated as:

$$SCA'_i = SC'_{i,D_{max}} - SC'_{i,D_{min}} \tag{2}$$

The pseudo SCA was defined to account for the difference in timing of the local D_{max} and D_{min} of the individual tracers and observed CH$_4$ at the observation sites. The total change in SCA over the study period, ΔSCA (ppb), was derived by calculating the linear trend (k_{SCA}) in the SCA and multiplying it by the number of years in the study (n_{year}, 25 years):

$$\Delta SCA = k_{SCA} \times n_{year} \tag{3}$$

Once the SCA and ΔSCA were calculated the surface sites were then grouped into five latitude bands for further analysis. These groups are Northern High Latitudes (NHL, 60°N-90°N), Northern Mid Latitudes (NML, 30°N-60°N), Northern Tropics (NTr, 0°-30°N), Southern Tropics (STr, 0°-30°S) and Southern High Latitudes (SHL 60°S-90°S). There are no surface observations from the Southern Mid Latitudes (SML, 30°S-60°S) so we do not analyse the SCA in this latitude band.

The main sink of CH$_4$ is through reaction with OH and the rate of removal is dependent on temperature and the amount of CH$_4$ and OH in the atmosphere (Dlugokencky et al., 1997). The atmospheric burden of CH$_4$ has been increasing and it is expected that the SCA of CH$_4$ would increase due to more CH$_4$ being removed by OH in the atmosphere, assuming that OH concentrations remain relatively constant during this time. To account for the impact of OH on ΔSCA we calculated the amount of CH$_4$ lost by OH across the whole atmosphere in each month of the study period:

$$L_{CH_4} = m_{CH_4}(1 - e^{-k[OH]\Delta t}) \tag{4}$$

$$k = 2.45 \times 10^{-12} e^{(-1775/T)} \tag{5}$$

Where L_{CH_4} is the amount of CH$_4$ lost (kg) in each model grid box through the reaction with OH in one month and m_{CH_4} is the mass of CH$_4$ in kg in each grid box. The variable k is the reaction rate constant (in cm^{3}molecules^{-1}s^{-1}, Equation 5 where T is temperature in Kelvin), [OH] is the amount of OH (molecules cm^{-3}) and Δt is number of seconds in one month. L_{CH_4} was converted to ppb and a mean monthly loss was calculated for the northern and southern hemisphere, across all the vertical model levels over the study period. The loss was then smoothed and detrended using the CCGCRV curve fitting routine and ΔSCA was calculated using the same method described above. It is not realistic to account for the contribution to ΔSCA from loss by OH at individual surface sites because this would not capture the seasonal cycle of OH in the mid-troposphere, where the majority of CH$_4$ loss by OH occurs. This makes it difficult to relate the seasonal changes in CH$_4$ due to loss by OH at particular sites, hence why we have calculated L_{CH_4} as a mean across the northern and southern hemispheres.
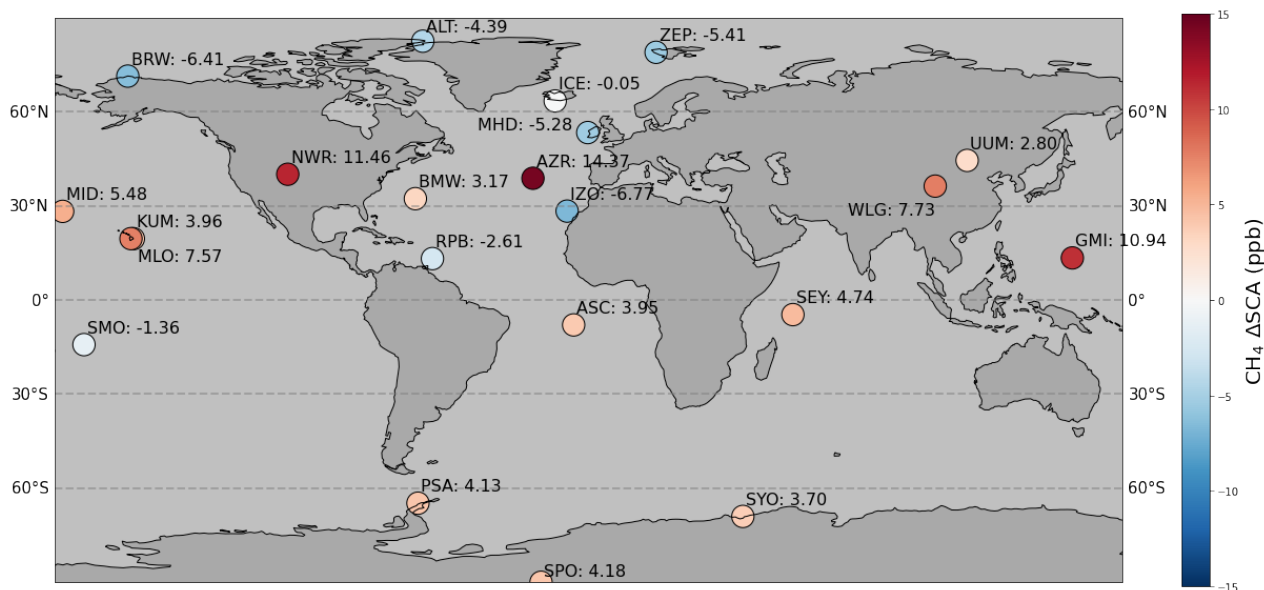
Figure 3. Map showing ΔSCA (ppb) at the 22 selected observation sites.

3 Results

3.1 Observed ΔSCA

205 The observed ΔSCA was calculated at the 22 observations sites. We find that the SCA is increasing globally but there are different regional trends, for example in the NHL the observed ΔSCA decreased at all sites between 1995-2020 (Fig. 3). The observed global mean value of ΔSCA was 2.5 ppb, corresponding to an increase of the SCA by 6.5%. However, the mean observed ΔSCA in the NHL was -4.0 ppb which is a 7.6% decrease between 1995-2020.

The distribution of ΔSCA at sites in Non-NHL regions is quite variable. For example at NWR, AZR and GMI ΔSCA is
210 large and positive but other sites such as MHD, IZR and SMO have negative ΔSCA values. The sites with the largest positive ΔSCA (e.g. NWR, BMW and AZR, GMI and WLG) are most likely influenced by outflow from the USA and Asia. The sites with large positive ΔSCA and negative ΔSCA in the Non-NHL regions do not have a strong regional or local pattern in ΔSCA, unlike in the NHL. Therefore, the NHL will be the main focus of our analysis. The Non-NHL regions had a mean observed ΔSCA of 4 ppb which is an increase of 11.5% for the study period. The three SHL sites sample well-mixed air and are less
215 influenced by local sources. The concentrations at regional sites near to emissions are all affected in different ways, whereas at the sites in Antarctica the effect is smoothed out by the time air reaches the South Pole region. The 3 sites in Antarctica are exposed to well-mixed air and have the same mean increase of 4 ppb, highlighting that the observed ΔSCA in NHL is very different to the global observed ΔSCA. This implies that the Arctic is responding differently to the global increase in CH$_4$ concentrations and therefore we focus on investigating the decreasing SCA in the NHL.
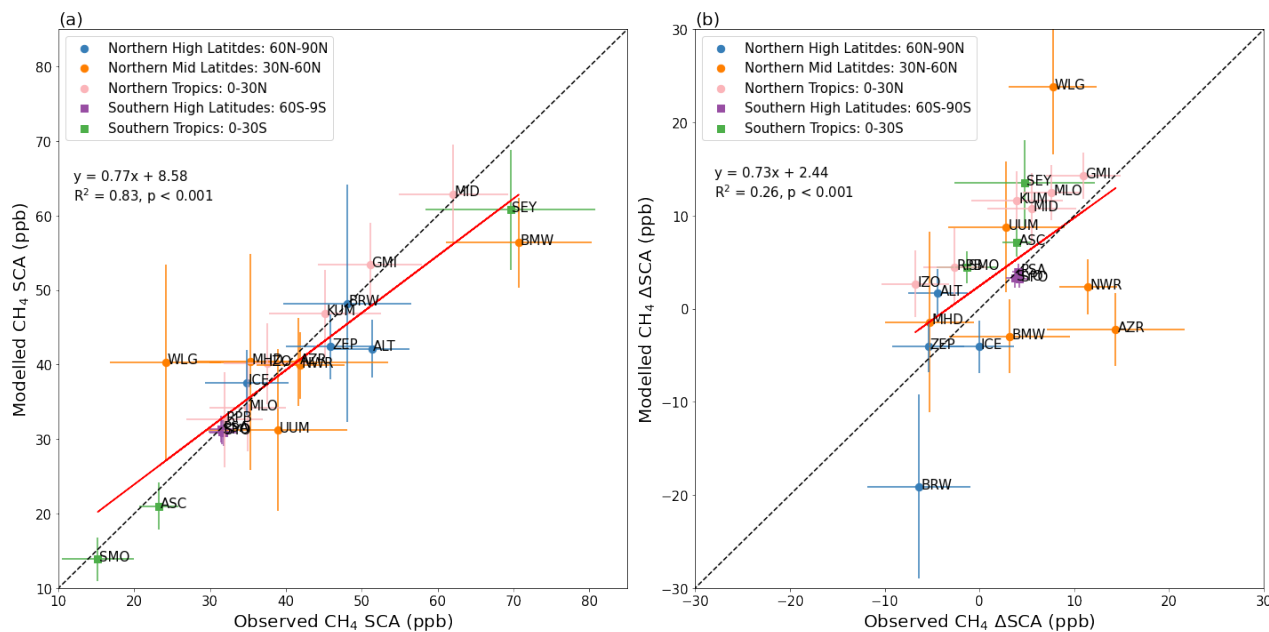
Figure 4. Comparison between simulated and observed (a) CH_4 SCA (ppb) and (b) CH_4 ΔSCA (ppb). The dashed black line represents the 1:1 line and the red line represents the least squares regression line, respectively. The error bars denote $\pm 1\sigma$.

220   3.2   Model Evaluation

The observed CH_4 SCA is simulated well by TOMCAT with the surface fluxes from INVICAT in the TOM_regional simulation (Fig. 4a). There is a strong linear relationship between the modelled and observed SCA with a mean bias of 0.93 ± 0.09 ppb. However, the model struggles to capture the SCA at Mount Waliguan (WLG) in China. This is likely due to the fact that it has the highest altitude out of all the sites and the reasonably coarse model grid cell will not capture the local topography. The model

225   simulation was also compared with sites that were not assimilated in INVICAT, although there are limited observations with only 6 sites situated in the Northern Tropics and Northern Mid Latitudes. Due to these sites only having regular observations over a short time period, the comparison only covers the periods 1997-2015 and 2009-2015 (see Supplement). The model captures the SCA well at these independent sites, apart from Cape Ochi-ishi (COI) where the model has a weaker seasonal cycle, particularly during the seasonal cycle minimum. COI is situated near swamps, grazing lands and two cities, so it is

230   possible that the model does not fully capture the complexity of the local sources well. There are large error bars (1σ) for the Siberian sites in both the modelled and observed SCA. This is due to the SCA being quite variable over the short time period available. However, the model still compares well with the observed SCA at these sites, with a mean overestimation of 16 ppb which is well within the 1σ error. Full results of the independent analysis can be found in the Supplement, Fig. S1. The model captures the mean SCA when compared with NOAA observation sites well but there are larger differences with the

235   independent sites, which is due, in part, to larger variability in the SCA over a shorter time period.

The model also captures ΔSCA well when compared with observations, including the negative ΔSCA in the NHL shown by observations (Fig. 4b). There is a good correlation (r=0.51) between the model and observations and they almost always match within the uncertainty, with some outliers. In the STr and NTr the model generally overestimates ΔSCA when compared with observations, however BMW, NWR and AZR are underestimated. In the SHL the model performs well against observations

240 with a slight overestimation of ΔSCA by an average of 0.5 ppb. In the NML the model over- or under-estimates ΔSCA at a number of sites when compared with the observations but agreement is usually within the uncertainty. At WLG the model overestimates ΔSCA, again this is likely due to the model representation at this site. The ΔSCA at BMW and NWR is generally underestimated with the largest difference towards the end of the study period, resulting in a smaller ΔSCA at these sites (See Supplement, Fig. S2). The SCA at AZR is overestimated at the beginning of the study period but underestimated towards the

245 end which results in a smaller ΔSCA when compared with observations. At ALT, TOMCAT shows a ΔSCA of 1.7 ppb and this is due to TOMCAT underestimating the SCA when compared with observations, particularly at the beginning of the study period. At BRW the model has a much stronger negative ΔSCA when compared with the observations and this is due to the model overestimating the SCA at the beginning of the study period. Despite the under- and over-estimations at the two sites in the NHL the mean value of ΔSCA in TOMCAT is -6.38 ppb in the NHL, which shows a larger negative trend in the SCA than

250 the observed mean ΔSCA value of -4 ppb. This is mostly due to the underestimation of ΔSCA at BRW. The time series of the SCA and its trend at each NOAA site can be found in the Supplement. The model captures the significantly different ΔSCA in the NHL relative to the rest of the globe so we can use it to inform on what might be causing this behaviour.

3.3 The Role of OH

We use the TOM_regional simulation to determine the influence the increasing abundance of CH_4 in the atmosphere has on its

255 removal by OH and the seasonal cycle. In the TOM_regional simulation we use OH fields which vary month to month but do not vary from year to year due to uncertainty in the annual variability. Some studies find a declining trend in OH from 2004 (Rigby et al., 2017; Turner et al., 2017) but Zhao et al. (2019) found an increasing trend in OH between 2000 and 2010. In contrast some studies only find small annual variability in OH (Patra et al., 2021; Naus et al., 2021). These studies contain large uncertainties and do not cover the full period of our study so a year to year variability in OH was not included our TOMCAT

260 simulations.

We find in the northern hemisphere the ΔSCA due to OH loss is +1.0 ppb, and +1.1 ppb in the southern hemisphere. From this, we would expect the observation sites to show a ΔSCA of ∼1 ppb in the absence of any other changes, and any deviations from that are due to changes in transport and/or emissions.

3.4 Regional Contribution to ΔSCA

265 We now assess what is driving the decreasing SCA in the NHL by analysing the regional contributions at NHL sites in the TOM_regional simulation. Figure 5 shows the contribution of the background and tagged regions as a mean across all sites in each latitude band. The background tracer shows the largest contribution to negative ΔSCA in the NHL (-9.93 ppb, Fig. 5a). The background tracer represents CH_4 that is well-mixed in the atmosphere, likely from emissions from distant regions.
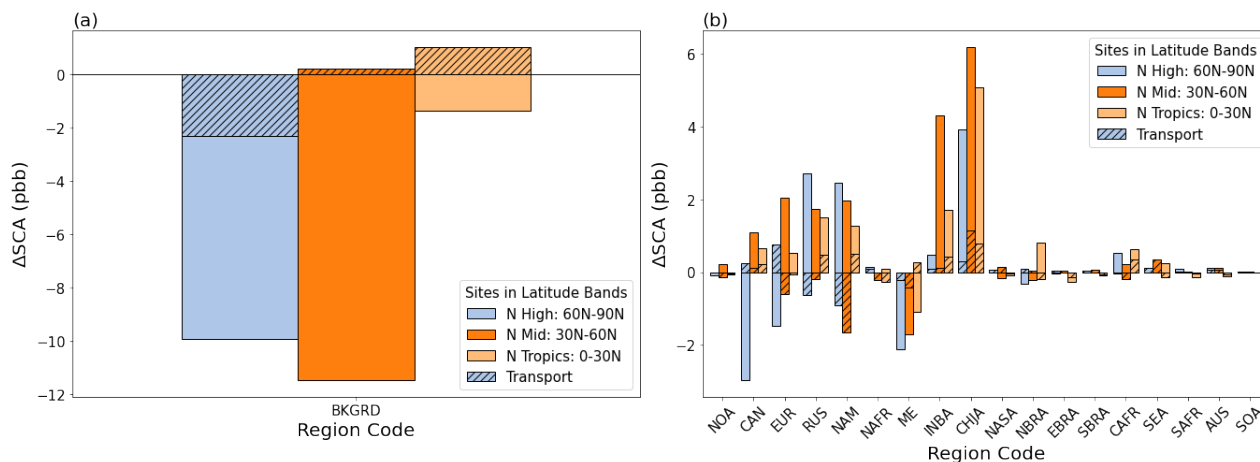
Figure 5. The contribution of the (a) background tracer (BKGRD) and (b) regional tagged tracers to CH$_4$ ΔSCA (ppb) as a mean across all sites in the latitude band. The hatched bars show the contribution from transport (TOM_transport) and the solid colour represents the contribution from emissions (TOM_regional).

The largest regional contributors to the negative ΔSCA in the NHL include Canada (-2.97 ppb), Middle East (-2.13 ppb) and

270 Europe (-1.48 ppb), shown in Fig. 5b. The China & Japan region has the largest positive influence on NHL ΔSCA (3.94 ppb). Despite some positive regional contributions of ΔSCA to the NHL, the ΔSCA in the NHL is still decreasing. This is due to the negative contribution of well-mixed emissions from the background tracer and large regional negative contributions from Canada, Europe and the Middle East.

The TOM_transport simulation represents the contribution of transport to the negative ΔSCA in the NHL and this simula-

275 tion shows a different regional contribution compared to the TOM_regional simulation (Fig. 5, TOM_transport simulation is represented by the hatched bars). From this simulation we find that 33% of the negative ΔSCA in the NHL is due to changes to transport and this can be split into contributions from the background and regional tracers. The largest contribution from transport as a fraction of the total contribution of the tracer is from the background tracer which accounts for 23% (-2.32 ppb). Changes in the transport of emissions from North America and Russia have also contributed to the decrease in the SCA

280 between 1995-2020 in the NHL, however the changes in emissions from these regions are so large, the overall result is a positive contribution to the NHL ΔSCA. The TOM_transport simulation also shows that the remaining contributions to the NHLs are due to changes in emissions. The TOM_transport contribution to ΔSCA in NHL from Canada and Europe is 0.24 ppb and 0.77 ppb respectively which is a smaller positive contribution compared to the larger negative contribution shown in the TOMCAT_regional simulation. This implies that their contributions to the negative ΔSCA in NHL are due to chnages in

285 emissions.

To further investigate the changes in emissions that are driving the negative ΔSCA in the NHL we look at the trends of the regional CH$_4$ concentration (ppb) contributions from the TOM_regional and TOM_transport simulation as a mean across all sites in the NHL. We also assess the trends of the seasonal emissions from each region. Often the trends in both the CH$_4$
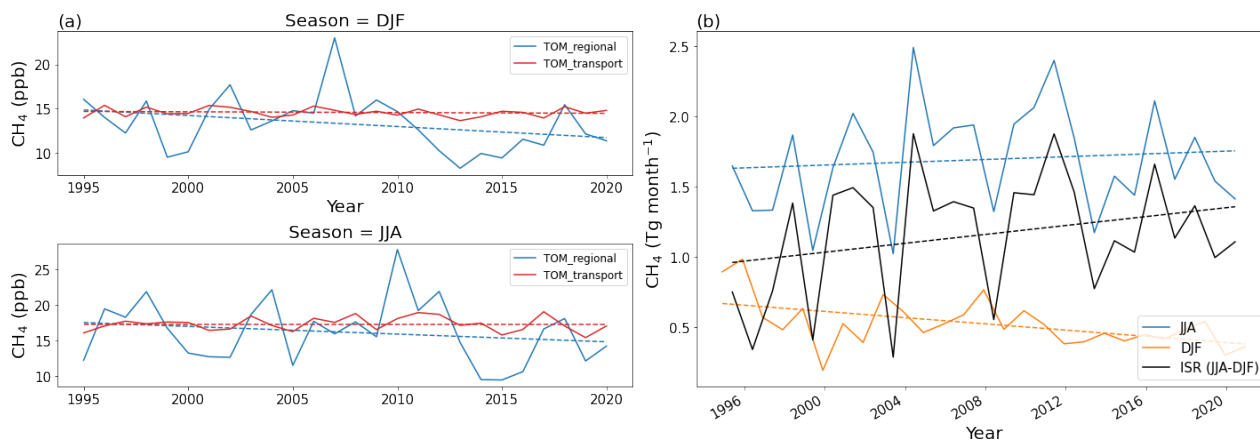
Figure 6. (a) Canada's seasonal mean CH_4 (ppb) contribution to the NHL sites (60N-90N) for TOM_regional (blue) and the TOM-CAT_transport simulation (red). (b) Canada's seasonal mean emissions (Tg month^{-1}) from the inversion for JJA (blue), DJF (orange) and the interseasonal range (ISR, black).
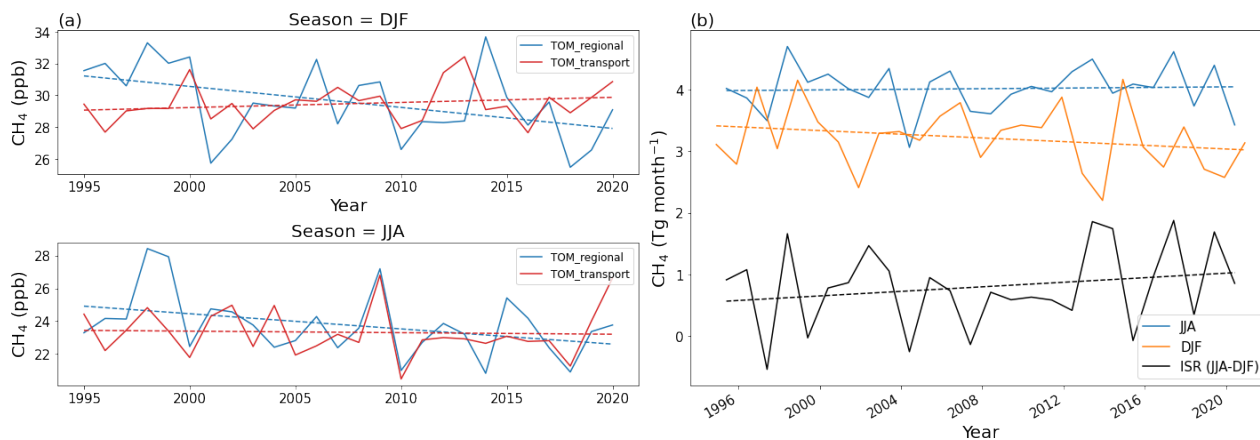
Figure 7. (a) Europe's mean CH_4 (ppb) contribution to the NHL sites (60N-90N) for the TOMCAT_regional (blue) and the TOM-CAT_transport simulation (red). (b) Europe's mean emissions (Tg month^{-1}) from the inversion for JJA (blue), DJF (orange) and the interseasonal range (ISR, black).

contributions and the regional emissions are not statistically significant due to their large variability over time. However, we
290 are interested in the direction of these trends in order to determine how emissions and transport from each region are changing over time and their impact on the seasonal cycle in the NHL. We compare the seasonal trends of regional contribution (in ppb) to the NHL from the TOMCAT_regional and TOMCAT_transport to further assess the contribution of emissions and transport from individual tracers. If the trend in the TOMCAT_transport simulation is comparable to the trend in the TOMCAT_regional simulation we can attribute the change to transport and not emissions. To assess the change in the seasonal emissions we

calculated the inter-seasonal range (ISR, Tg month^{-1}) which represents the difference between June, July, August (JJA) and December, January, February (DJF) seasonal mean emissions. It is important to note that the emission seasonal cycle is not synchronised with the concentration seasonal cycle at northern mid- and high-latitudes, so a positive ISR in emissions leads to a decreasing SCA. For example, when summer emissions increase and winter emissions decrease, this results in a positive ISR and decreasing SCA. This is because the CH_4 concentration at the seasonal cycle minimum will be higher in summer due to the increasing emissions. This is due to more CH_4 being present in the atmosphere during the period of maximum chemical loss. The CH_4 concentration at the seasonal cycle maximum will be smaller due to decreasing emission, due to less CH_4 being emitted into the atmosphere during the period of maximum concentrations. The combination of increasing summer emissions and decreasing winter emissions impacts the SC maximum and SC minimum concentrations, resulting in a smaller SCA. We focus on the three largest regional contributors to the negative ΔSCA in the NHL: Canada, Europe and the Middle East. We also focus on the largest regional positive contributor of ΔSCA in the NHL, China & Japan, to assess its impact on the decreasing SCA at NHL sites.

Figure 5 shows that changes in transport from Canada contribute to a positive ΔSCA at the NHL sites. However, changes in Canadian emissions from TOM_regional simulation contributes to a negative ΔSCA to the NHL sites. The mean CH_4 concentration contribution across the NHL from Canada in the TOM_transport simulation shows no strong trends during the DJF seasons (Fig. 6a). The trend of the DJF concentrations contribution in the TOM_regional is decreasing at a faster rate (-0.13 ppb month^{-1}, pvalue = 0.13) than the JJA (-0.11 ppb month^{-1}, pvalue = 0.36), which results in a decrease in the SCA. This is because the annual maximum concentrations are decreasing at a faster rate than the annual minimum and, as a result, the SCA decreases. Figure 6b shows that the JJA emissions from Canada are increasing and the DJF emissions are decreasing, leading to a positive ISR (0.02Tg month^{-1} year^{-1}, pvalue=0.17). The combination of weak trends in TOM_transport simulation and the positive ISR indicates that changes in DJF and JJA emissions from Canada is the main contributor to the decreasing SCA in this region.

Similarly, Fig. 5 shows that changes in transport from Europe contributes to a positive ΔSCA to the NHL sites. However, changes in European emissions from TOM_regional contributes to a negative ΔSCA to the NHL sites. The mean CH_4 concentration contribution from Europe to the NHL sites in the TOM_transport simulation shows a small positive trend in DJF (0.03 ppb month^{-1}, pvalue = 0.3) and a very small decreasing trend in JJA (-0.009 ppb month^{-1}, pvalue = 0.38, Fig. 7a). This shows that changes in winter transport are contributing to an increase in the SCA in the NHL. However, the changes in emissions shows in the TOM_regional simulation contribute more to a decrease in the SCA. The TOM_regional DJF (-0.13 ppb month^{-1}, pvalue=0.02) and JJA (-0.09 ppb month^{-1}, pvalue=0.06) trends are decreasing across the NHL (Fig. 7a). The DJF concentrations from Europe are decreasing at a faster rate than the JJA concentrations, resulting in an decrease in the SCA. The emissions from Europe during JJA are increasing slightly but there is a stronger decrease in the DJF emissions. The decrease in winter emissions result in a positive ISR (0.02 Tg month^{-1} year^{-1}, pvalue=0.3, Fig. 7b). The combination of the positive ISR and because the DJF concentrations in TOM_regional are decreasing at a faster rate than the JJA concentrations in the NHL from Europe indicates that emissions are contributing to a decreasing SCA.
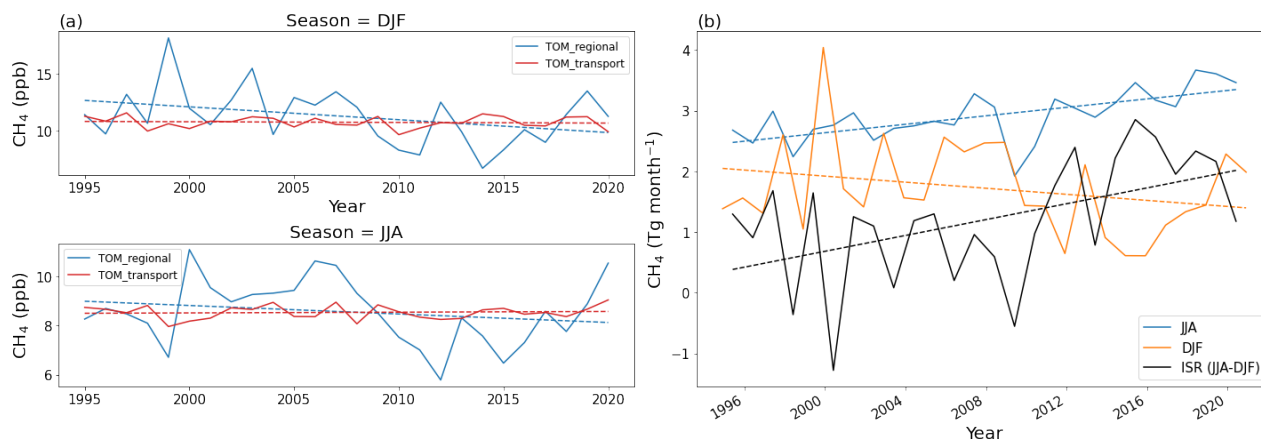
Figure 8. (a) The Middle East's mean CH$_4$ (pbb) contribution to the NHL sites (60N-90N) for the TOM_regional simulation (blue) and the TOM_transport simulation (red). (b) The Middle East's mean emissions (Tg month^{-1}) from the inversion for JJA (blue), DJF (orange) and the interseasonal range (ISR, black).

The Middle East contribution to the negative ΔSCA in the NHL is driven mainly by changes in emissions (Fig. 5). The

330   mean CH$_4$ concentration contribution from the Middle East to the NHL sites is decreasing in both JJA (-0.04 ppb month^{-1}, pvalue=0.3) and DJF (-0.11 ppb month^{-1}, pvalue=0.07) in the TOM_regional simulation (Fig. 8a). The trend in DJF is decreasing faster than the trend in JJA, resulting in a decrease in the SCA. There is no trend in the TOM_transport simulation for DJF and JJA, meaning that transport has had very little impact on the change in the SCA. The emissions from the Middle East are increasing in JJA and decreasing in DJF, which results in a positive ISR (0.07 Tg month^{-1} year^{-1}, pvalue=0.01, Fig. 8b).

335   The comparison of the TOM_transport and TOM_regional simulations and the positive ISR show that changing emissions are the main contributor from the Middle East to the decreasing SCA in the NHL.

The largest positive contribution to ΔSCA in the NHL is from China & Japan. The mean CH$_4$ concentration contribution from this region to the NHL is increasing in DJF and JJA in the TOM_regional simulation (Fig. 9a). The DJF contribution is increasing at a faster rate (0.15 ppb month^{-1}, pvalue=0.03) than the JJA contribution (0.07 ppb month^{-1}, pvalue=0.21), result-

340   ing in an increase in the SCA. The TOM_transport simulation shows a small trend in DJF (0.015 ppb month^{-1}, pvalue=0.32) in the concentration contribution from this region and no trend in the JJA contribution, showing that transport is also contributing to an increase in the SCA in NHL. The emissions from China & Japan are decreasing slightly in JJA and increasing in DJF, resulting in a negative ISR (-0.07 Tg month^{-1} year^{-1}, pvalue=0.05, Fig. 9b). The TOMCAT simulations and emissions show that changes in emissions and DJF transport from China & Japan contributes to an increase in the SCA in the NHL. However,

345   the overall contribution from the background tracer and other regional tracers still results in a decrease in the SCA in the NHL.
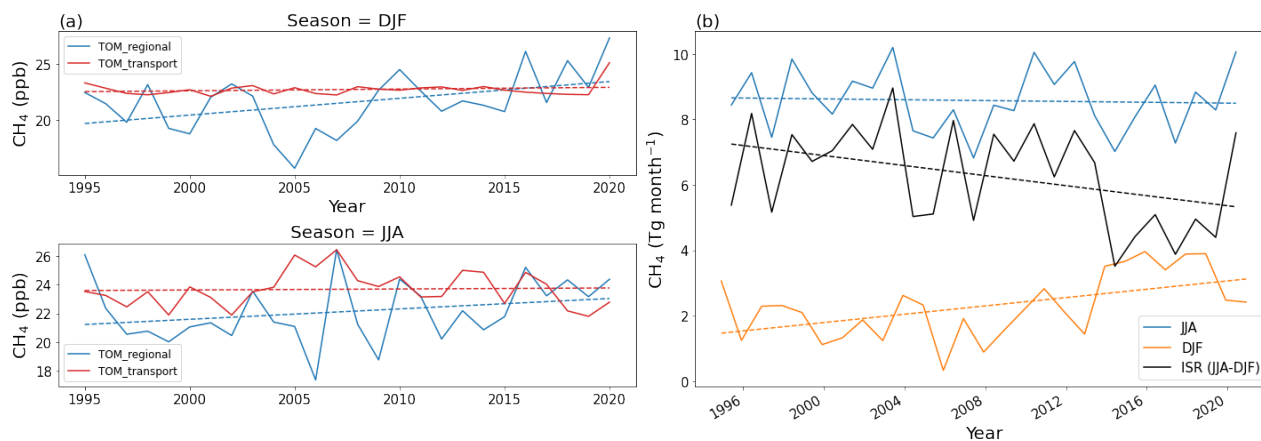
Figure 9. (a) shows China & Japan's mean CH$_4$ (pbb) contribution to the NHL sites (60N-90N) for the TOMCAT_regional (blue) and the TOMCAT_transport simulation (red). (b) shows China & Japan's mean emissions (Tg month^{-1}) from the inversion for JJA (blue), DJF (orange) and the interseasonal range (ISR, black).

3.5 Sensitivity Experiments

We carried out two sensitivity experiments to examine the impact of shorter and longer decay rates of regional tracers into the background tracer. These simulations are described in Sect. 2.2. The TOM_twelve simulation showed that changing the exponential decay rate from 9 months to 12 months did not change the largest contributors to the ΔSCA. This implies that

350 after 9 months, CH$_4$ emissions has undergone long-range transport and no longer has a distinguishable emission origin, so has become well-mixed. Reducing the exponential decay rate to 1 month did, however, have an impact on the final results. The TOM_one simulation showed larger regional contributions in the NHL from Canada than the background tracer. The contribution from the background tracer in the TOM_one simulation contains emissions from southern regions because emissions from these regions will have been moved into the background tracer before they had the chance to reach the NHL. For regions

355 close to the NHL sites, such as Canada and Russia, we can see the effect of those emissions before they become well-mixed. The recent local emissions from Canada are having an impact on the decreasing SCA but the effects of mixing and changes in transport will reduce this impact. These sensitivity experiments show that the 9-month decay rate into the background is a good compromise for quantifying well-mixed emissions. It allows us to look at the effect from relatively recent emissions and also allows enough time for far-away emissions to be transported to the NHL in order to quantify their effect on the ΔSCA.

360 More details on the sensitivity study can be found in Appendix A.

4 Discussion

Using the NOAA surface observations we have shown that globally the SCA of CH$_4$ is increasing but in the NHL it is decreasing. As the atmospheric burden of CH$_4$ is increasing it would be expected that the SCA would show a corresponding increase

due to greater removal of CH_4 by OH in the atmosphere. Therefore, the change in the SCA in the NHL is counter-intuitive and we explore through TOMCAT simulations what is driving this decreasing SCA. A persistent change in the SCA indicates a long-term change in the sources, sinks and/or transport of CH_4, and the decreasing SCA in the NHL indicates a different response to the increasing atmospheric CH_4 burden compared to the rest of the world.

We use a TOMCAT-based atmospheric inversion which assimilates NOAA surface observations across the globe. There is a much greater number of sites situated in the northern hemisphere, compared with the southern hemisphere. There are large and variable sources of CH_4 in central Africa and Brazil but the model is not well constrained over these regions due to the lack of observations. The large contribution of emissions to the global CH_4 budget from central Africa and Brazil has been highlighted in a number of recent studies (Lunt et al., 2021; Wilson et al., 2021; Feng et al., 2022) so the surface emissions in our study might not fully capture the magnitude and distribution of emissions from these regions due to the lack of observations.

The TOMCAT tagged tracer simulations do capture ΔSCA when compared with observations and we can use the model to regionally attribute the change in the SCA. However, it is difficult to disaggregate the contribution of different emission types within these regions. When possible, we have estimated emission types by looking at emission maps of each of the largest regional contributors and referring to literature. In addition to regional contributions, the regional tracers were allocated to a background tracer using an exponential 9-month decay rate to represent well-mixed methane that no longer has a distinguishable emission origin. It is not possible to tell from our simulations what regions are contributing the most to the background tracer.

We have shown through TOMCAT simulations that well-mixed (background) CH_4, likely from emissions from regions far from the NHL, along with regions in the lower northern latitudes, are having a large influence on the SCA in the NHL. Whilst transport from the background tracer is a contributing factor to the decrease in the SCA in the NHL, 83% of all tracer contributions are due to emissions. Here we discuss the emissions sectors that might be driving these seasonal changes from the largest regional contributors to the change in the SCA in NHL. These include Canada, Europe, Middle East and China & Japan.

Canada has the largest negative contribution to the ΔSCA NHL due to emissions (-2.97 ppb). An increase in JJA and a decrease in DJF emissions have impacted the CH_4 contribution in the NHL, leading to a decrease in the SCA. There are a number of different sources which could contribute to the changes in emissions in Canada. Anthropgenic sources of CH_4 in Canada include oil and gas, livestock and landfills and natural sources include wetlands and biomass burning (Scarpelli et al., 2021). Studies investigating the seasonality of the Hudson Bay Lowlands, the second largest boreal wetland in the world, found the wetland emissions peak in July/August and decreases significantly in September-to-November (Pickett-Heaps et al., 2011; Fujita et al., 2018). Fujita et al. (2018) also found that biogenic sources are the most dominant for the seasonal cycle in this region and that the boreal wetlands are the main source. They found that fossil fuels and biomass burning are minor contributors to the CH_4 concentration seasonal cycle. Fossil fuels are often classed as a nonseasonal source but Fujita et al. (2018) find that they contribute significantly to the mole fraction of CH_4 in early winter at the Churchill observation site situated on Hudson Bay's coast. This implies that fossil fuel emissions have some seasonality in this region, peaking in winter. Scarpelli et al. (2021) report that top-down estimates from satellite data show a decreasing trend in emissions for 2010-2017. The emissions

used in our model show a decrease annually in September, indicating the wetlands are a large factor in this region's season cycle. The mean seasonal emissions for the study period peak in JJA over western Canada which is an area prone to wildfires and emissions are also large around the Boreal Plains (Environment and Climate Change Canada, 2016). Also the GFED fire emissions database (van der Werf et al., 2017) shows that annual emissions of CH_4 from biomass burning have been increasing from 1997-2020 (0.03 Tg year^{-1}, pvalue=0.01, see Supplement Fig. S7). Despite the emission trends in our results having high pvalues, the direction of the trends follow changes reported by literature. It is likely that wetland and biomass burning emissions are increasing during the summer in Canada, contributing to the negative ΔSCA contribution to the NHL, with some influence of decreasing anthropogenic emissions in the winter. The positive trends in emissions are often over wetland and biomass burning regions during summer and the winter decrease in emissions is strongest in western Canada where there are a few main cities (See Supplement, Fig. S3b).

The Middle East region has the second largest contribution to the decreasing SCA in the NHL (-2.13 ppb). The trend in the ISR of emissions from the Middle East has a pvalue of 0.01 which further implies that emissions are responsible for the contribution to the negative ΔSCA in NHL. Emissions in this region are dominated by anthropogenic emissions such as oil and gas, agriculture and waste. A recent study has shown that the Middle East is one of the largest contributors to the rise in CH_4 emissions between 2000 and 2017 (Stavert et al., 2022). Our emission maps show the largest emissions in JJA, particularly over the Caspian Sea and the Persian Gulf, which is a region of significant oil and gas extraction. The seasonality of emissions from this region is not well documented so it is not possible to be certain of the change in emissions in this region that is contributing to the decreasing SCA in the NHL. The emissions used in the model indicate the largest increases in emissions in JJA and decreases in DJF emissions are in areas known for oil and gas extraction (Supplement, Fig. S4b). From this, it is likely that anthropogenic emissions are driving the changes in contribution to the decrease in SCA in the NHL from this region.

Europe is the third largest contributor to the decrease in the SCA in the NHL (-1.48 ppb). The TOM_regional JJA and DJF trends in the concentration contributions to the NHL from this region are 0.06 and 0.02, respectively. This highlights that it is mostly emissions contributing to the decrease in the SCA in this region. Emissions in Europe include natural sources such as wetlands, peatlands and wet soils, and anthropogenic emissions such as agriculture, waste and fossil fuels (Bergamaschi et al., 2018). It is often assumed that wetlands have the strongest seasonality and Bergamaschi et al. (2018) explained that precipitation is important for southern European wetlands but temperate and boreal wetlands are driven by temperature variations. Southern European wetlands could be impacted by a decreasing trend in precipitation shown by Christidis and Stott (2022), which could result in a decrease in wetland emissions. It is hard to say what emission types are driving the decrease in winter emissions over Europe due to lack of studies of the seasonality of sources in this region; it is possible that sources other than wetlands are having an impact. For example, improvements in the efficiency of fossil fuel use, domestic and/or extraction could result in lower CH_4 emissions in winter.

China & Japan is the region which contributes the most to an increase in the SCA in the NHL. The DJF concentration contribution has a pvalue of 0.02 so it is likely that this season is driving this positive contribution. Emissions in China & Japan are mostly driven by agriculture and waste and fossil fuels (Stavert et al., 2022). Stavert et al. (2022) found that fossil fuel emissions have increased by 114% in bottom-up estimates and 78% in top-down estimates between 2000 and 2017.

The differences arise due to the emission inventories diverging towards the end of their study period. However, this does show that fossil emissions from China have increased significantly over the last two decades. Approximately 40% of China's anthropogenic emissions are from fossil fuels and the remainder is split equally between livestock, rice paddies and waste (Stavert et al., 2022). Our emissions show the largest emissions are situated in south east China (Supplement, Fig. S6) where rice paddies, oil and gas, and waste are the main sources of CH_4 (Peng et al., 2016). Despite the fact that emissions are generally increasing in China and causing a large positive contribution to ΔSCA in the NHL, the SCA in the NHL is still decreasing.

The three main regions that contribute the most to the decreasing SCA in the NHL (Canada, Europe and Middle East) have common trends in emissions and concentration contributions to the NHL sites. The trends in regional concentration contributions across the whole of the NHL at the surface show similar results (See Supplement). In each region the winter emissions are generally decreasing and summer emissions are increasing over the study period. Similarly the regional DJF concentration contribution to the NHL generally decreases at a faster rate than the JJA concentration contribution, resulting in a decrease in the SCA, despite the fact that emissions from the region are increasing in JJA. This is likely due to a redistribution of emissions over time from each region, causing it to be transported differently to the NHL. We have shown that changes in well-mixed emissions and changes in emissions from Canada, Europe and the Middle East are the main contributors to the decreasing SCA in the NHL. The results show that the CH_4 SCA is changing and this should act as motivation to investigate the seasonality of emissions as it highlights changes in the CH_4 budget.

5 Conclusions

We have used a 3-D chemical transport model, TOMCAT, with emissions derived from surface observations, to investigate changes in the SCA of CH_4. Using TOMCAT we find that the global mean SCA increased by 1 ppb between 1995-2020 due to the increase in atmospheric CH_4 but this is offset by changes in emissions and transport. The NOAA surface observations show that globally the SCA has increased by a mean value of 2.5 ppb (6.5%) but decreased by 4 ppb (7.6%) in the NHL. The decreasing SCA in the NHL therefore does not follow the global trend and indicates that the seasonal cycle is responding differently to the global increase in atmospheric CH_4.

Our study focused on what was driving the decrease in the SCA in the NHLs and found that well-mixed methane, allocated to a modelled background tracer, was the largest contributor. Around 33% of the background tracer's contribution to the NHL could be attributed to changes in transport whilst the remaining contribution is from emissions. The background tracer contains CH_4 that has become well-mixed and no longer has a distinguishable emission origin. Emissions from distant regions are likely to be main contributors to the background tracer as it is transported to the NHL. The largest regional contributions to the negative ΔSCA in the NHL are from Canada, Europe and the Middle East. Increases in summer emissions from the Boreal Plains in Canada, decreases in winter emissions across Europe, and a combination of increases in summer emissions and decreases winter in emissions over the Arabian Peninsula and Capsian Sea in the Middle East are the other main contributors to the decrease in the SCA in the NHL.

The lack of studies that investigate the seasonality of emissions makes it hard to determine the source sector that is driving the change in emissions in these regions. The changes in the SCA in the NHL and globally indicate a long-term change in sources of CH_4 and highlight the seasonal response to the increasing CH_4 burden. More work is needed to investigate the seasonality of the sources that are having an impact on the decreasing SCA in the NHL.

470 *Code and data availability.* The NOAA data (Dlugokencky et al., 2021) are available from https://doi.org/10.15138/VNCZ-M766 (last access: 2nd December 2021). The AGAGE data (Prinn et al., 2018) are available from https://doi.org/10.3334/CDIAC/atg.db1001 (last access: 26th May 2022). The observations for Cape Ochi-ishi can be found at https://doi.org/10.17595/20160901.004 and Hateruma Island can be found at https://doi.org/10.17595/20160901.003 (last access: 8th November 2021). The Siberian tower observations are available through registration at the Global Environmental Database https://db.cger.nies.go.jp/ged/en/ (last accessed: 19th October 2022). The GFED fire emis-
475 sions (van der Werf et al., 2017) can be found at https://www.globalfiredata.org/. The TOMCAT detrended time series at the 22 observation sites will be uploaded to the Zenodo open access portal (https://zenodo.org/) if this manuscript is accepted for publication in ACP after the peer-review process. Readers should contact the lead author to enquire about the use of the TOMCAT model.

Appendix A: Sensitivity Testing on Background Tracer

We carried out a sensitivity experiment on the exponential decay of the CH_4 tracer into the background. The results of these
480 model runs showed that changing the e-folding time (lifetime) from 9 months to 12 months did not have a large impact on the results. We also set the lifetime to 1 month, this did have an impact on the final results but 1 month lifetime is too short to represent well-mixed methane. Find the results of the model simulations in Table A1.

Author contributions. ED, CW, EG and MPC designed the study, ED carried out forward model simulations, inversions were carried about by CW, both with input from MPC. AM and RD provided guidance for data analysis. All co-authors contributed to the writing and analysis
485 of the results.

Competing interests. The authors declare that they have no conflict of interest.

Acknowledgements. This work was supported by the Natural Environment Research Council (NERC) SENSE CDT studentship (NE/T00939X/1). This work was also supported by NERC grants NE/V006924/1 and NE/V011863/1. We would like to thank NOAA GML CCGG for providing the long term, global surface observations. We would also like to thank M. Sasakawa and Y. Tohjima at the Center for Global Environmental
490 Research Earth System Division National Institute for Environmental Studies for providing the independent observations in Siberia and at Haterma and Ochi-ishi. The station at Mace Head (GC-MD) is supported by the UK Department of Business Energy and Industrial Strategy(BEIS) (Contract number:TRN1537/06/2018). The operation and calibration of the global AGAGE measurement network are supported

by NASA's Upper Atmosphere Research Program through grants NAG5-12669, NNX07AE89G, NNX11AF17G, and NNX16AC98G (to MIT) and NNX07AE87G, NNX07AF09G, NNX11AF15G, and NNX11AF16G (to SIO).

References

Basso, L. S., Marani, L., Gatti, L. V., Miller, J. B., Gloor, M., Melack, J., Cassol, H. L. G., Tejada, G., Domingues, L. G., Arai, E., Sanchez, A. H., Corrêa, S. M., Anderson, L., Aragão, L. E. O. C., Correia, C. S. C., Crispim, S. P., and Neves, R. A. L.: Amazon methane budget derived from multi-year airborne observations highlights regional variations in emissions, Communications Earth & Environment, 2, https://doi.org/10.1038/s43247-021-00314-4, 2021.

Bergamaschi, P., Karstens, U., Manning, A. J., Saunois, M., Tsuruta, A., Berchet, A., Vermeulen, A. T., Arnold, T., Janssens-Maenhout, G., Hammer, S., Levin, I., Schmidt, M., Ramonet, M., Lopez, M., Lavric, J., Aalto, T., Chen, H., Feist, D. G., Gerbig, C., Haszpra, L., Hermansen, O., Manca, G., Moncrieff, J., Meinhardt, F., Necki, J., Galkowski, M., O'Doherty, S., Paramonova, N., Scheeren, H. A., Steinbacher, M., and Dlugokencky, E.: Inverse modelling of European CH_4 emissions during 2006–2012 using different inverse models and reassessed atmospheric observations, Atmospheric Chemistry and Physics, 18, 901–920, https://doi.org/10.5194/acp-18-901-2018, 2018.

Bloom, A. A., Bowman, K. W., Lee, M., Turner, A. J., Schroeder, R., Worden, J. R., Weidner, R., McDonald, K. C., and Jacob, D. J.: A global wetland methane emissions and uncertainty dataset for atmospheric chemical transport models (WetCHARTs version 1.0), Geoscientific Model Development, 10, 2141–2156, https://doi.org/10.5194/gmd-10-2141-2017, 2017.

Chipperfield, M. P.: New version of the TOMCAT/SLIMCAT off-line chemical transport model: Intercomparison of stratospheric tracer experiments, Quarterly Journal of the Royal Meteorological Society, 132, 1179–1203, https://doi.org/https://doi.org/10.1256/qj.05.51, 2006.

Christidis, N. and Stott, P. A.: Human Influence on Seasonal Precipitation in Europe, Journal of Climate, 35, 5215–5231, https://doi.org/10.1175/JCLI-D-21-0637.1, 2022.

Crippa, M., Guizzardi, D., Muntean, M., and E, S.: EDGAR v5.0 Global Air Pollutant Emissions, http://data.europa.eu/89h/377801af-b094-4943-8fdc-f79a7c0c2d19, 2021.

Dlugokencky, E., Crotwell, A., Mund, J., Crotwell, M., and Thoning, K.: Atmospheric Methane Dry Air Mole Fractions from the NOAA GML Carbon Cycle Cooperative Global Air Sampling Network, 1983-2020, Version: 2021-07-30, https://doi.org/10.15138/VNCZ-M766, 2021.

Dlugokencky, E. J., Steele, L. P., Lang, P. M., and Masarie, K. A.: The growth rate and distribution of atmospheric methane, Journal of Geophysical Research: Atmospheres, 99, 17 021–17 043, https://doi.org/https://doi.org/10.1029/94JD01245, 1994.

Dlugokencky, E. J., Masarie, K. A., Tans, P. P., Conway, T. J., and Xiong, X.: Is the amplitude of the methane seasonal cycle changing?, Atmospheric Environment, 31, 21–26, https://doi.org/10.1016/S1352-2310(96)00174-4, 1997.

Environment and Climate Change Canada: Canadian Environmental Sustainability Indicators: Extent of Canada's Wetlands, accessed 25/10/2022, 2016.

Etiope, G., Ciotoli, G., Schwietzke, S., and Schoell, M.: Gridded maps of geological methane emissions and their isotopic signature, Earth System Science Data, 11, https://doi.org/10.5194/essd-11-1-2019, 2019.

Feng, L., Palmer, P. I., Zhu, S., Parker, R. J., and Liu, Y.: Tropical methane emissions explain large fraction of recent changes in global atmospheric methane growth rate, Nature Communications, 13, https://doi.org/10.1038/s41467-022-28989-z, 2022.

Fujita, R., Morimoto, S., Umezawa, T., Ishijima, K., Patra, P. K., Worthy, D. E. J., Goto, D., Aoki, S., and Nakazawa, T.: Temporal Variations of the Mole Fraction, Carbon, and Hydrogen Isotope Ratios of Atmospheric Methane in the Hudson Bay Lowlands, Canada, Journal of Geophysical Research: Atmospheres, 123, 4695–4711, https://doi.org/10.1002/2017JD027972, 2018.

Gloor, E., Wilson, C., Chipperfield, M. P., Chevallier, F., Buermann, W., Boesch, H., Parker, R., Somkuti, P., Gatti, L. V., Correia, C., Domingues, L. G., Peters, W., Miller, J., Deeter, M. N., and Sullivan, M. J. P.: Tropical land carbon cycle responses to 2015/16 El Nino as recorded by atmospheric greenhouse gas and remote sensing data, Philosophical Transactions of the Royal Society B: Biological Sciences,

535   373, 20170 302, https://doi.org/10.1098/rstb.2017.0302, 2018.

Hersbach, H., Bell, B., Berrisford, P., Hirahara, S., Horányi, A., Muñoz-Sabater, J., Nicolas, J., Peubey, C., Radu, R., Schepers, D., Simmons, A., Soci, C., Abdalla, S., Abellan, X., Balsamo, G., Bechtold, P., Biavati, G., Bidlot, J., Bonavita, M., De Chiara, G., Dahlgren, P., Dee, D., Diamantakis, M., Dragani, R., Flemming, J., Forbes, R., Fuentes, M., Geer, A., Haimberger, L., Healy, S., Hogan, R. J., Hólm, E., Janisková, M., Keeley, S., Laloyaux, P., Lopez, P., Lupu, C., Radnoti, G., de Rosnay, P., Rozum, I., Vamborg, F., Vil-

540   laume, S., and Thépaut, J.-N.: The ERA5 global reanalysis, Quarterly Journal of the Royal Meteorological Society, 146, 1999–2049, https://doi.org/https://doi.org/10.1002/qj.3803, 2020.

Huijnen, V., Williams, J., van Weele, M., van Noije, T., Krol, M., Dentener, F., Segers, A., Houweling, S., Peters, W., de Laat, J., Boersma, F., Bergamaschi, P., van Velthoven, P., Le Sager, P., Eskes, H., Alkemade, F., Scheele, R., Nédélec, P., and Pätz, H.-W.: The global chemistry transport model TM5: description and evaluation of the tropospheric chemistry version 3.0, Geoscientific Model Development,

545   3, 445–473, https://doi.org/10.5194/gmd-3-445-2010, 2010.

Lin, X., Rogers, B. M., Sweeney, C., Chevallier, F., Arshinov, M., Dlugokencky, E., Machida, T., Sasakawa, M., Tans, P., and Keppel-Aleks, G.: Siberian and temperate ecosystems shape Northern Hemisphere atmospheric CO2 seasonal amplification, Proceedings of the National Academy of Sciences, 117, 21 079–21 087, https://doi.org/10.1073/pnas.1914135117, 2020.

Lunt, M. F., Palmer, P. I., Lorente, A., Borsdorff, T., Landgraf, J., Parker, R. J., and Boesch, H.: Rain-fed pulses of methane from East Africa

550   during 2018–2019 contributed to atmospheric growth rate, Environmental Research Letters, 16, https://doi.org/10.1088/1748-9326/abd8fa, publisher: IOP Publishing, 2021.

McNorton, J., Wilson, C., Gloor, M., Parker, R. J., Boesch, H., Feng, W., Hossaini, R., and Chipperfield, M. P.: Attribution of recent increases in atmospheric methane through 3-D inverse modelling, Atmospheric Chemistry and Physics, 18, 18 149–18 168, https://doi.org/10.5194/acp-18-18149-2018, 2018.

555   Meirink, J. F., Bergamaschi, P., and Krol, M. C.: Four-dimensional variational data assimilation for inverse modelling of atmospheric methane emissions: method and comparison with synthesis inversion, Atmospheric Chemistry and Physics, 8, 6341–6353, https://doi.org/10.5194/acp-8-6341-2008, 2008.

Monks, S. A., Arnold, S. R., Hollaway, M. J., Pope, R. J., Wilson, C., Feng, W., Emmerson, K. M., Kerridge, B. J., Latter, B. L., Miles, G. M., Siddans, R., and Chipperfield, M. P.: The TOMCAT global chemical transport model v1.6: description of chemical mechanism and

560   model evaluation, Geoscientific Model Development, 10, 3025–3057, https://doi.org/10.5194/gmd-10-3025-2017, 2017.

Murguia-Flores, F., Arndt, S., Ganesan, A. L., Murray-Tortarolo, G., and Hornibrook, E. R. C.: Soil Methanotrophy Model (MeMo v1.0): a process-based model to quantify global uptake of atmospheric methane by soil, Geoscientific Model Development, 11, 2009–2032, https://doi.org/10.5194/gmd-11-2009-2018, 2018.

Naus, S., Montzka, S. A., Patra, P. K., and Krol, M. C.: A three-dimensional-model inversion of methyl chloroform to constrain the atmo-

565   spheric oxidative capacity, Atmospheric Chemistry and Physics, 21, 4809–4824, https://doi.org/10.5194/acp-21-4809-2021, 2021.

Nisbet, E. G., Dlugokencky, E. J., Manning, M. R., Lowry, D., Fisher, R. E., France, J. L., Michel, S. E., Miller, J. B., White, J. W. C., Vaughn, B., Bousquet, P., Pyle, J. A., Warwick, N. J., Cain, M., Brownlow, R., Zazzeri, G., M., L., Manning, A. C., Gloor, E., Worthy, D. E. J., Brunke, E.-G., Labuschagne, C., Wolff, E. W., and Ganesan, A. L.: Rising atmospheric methane: 2007–2014 growth and isotopic shift, Global Biogeochemical Cycles, 30, 1356–1370, https://doi.org/https://doi.org/10.1002/2016GB005406, 2016.

570   Nisbet, E. G., Manning, M. R., Dlugokencky, E. J., Fisher, R. E., Lowry, D., Michel, S. E., Myhre, C. L., Platt, S. M., Allen, G., Bousquet, P., Brownlow, R., Cain, M., France, J. L., Hermansen, O., Hossaini, R., Jones, A. E., Levin, I., Manning, A. C., Myhre, G., Pyle, J. A., Vaughn, B. H., Warwick, N. J., and White, J. W. C.: Very Strong Atmospheric Methane Growth in the 4 Years 2014–2017: Implications for the Paris Agreement, Global Biogeochemical Cycles, 33, 318–342, https://doi.org/https://doi.org/10.1029/2018GB006009, 2019.

Parker, R. J., Boesch, H., McNorton, J., Comyn-Platt, E., Gloor, M., Wilson, C., Chipperfield, M. P., Hayman, G. D., and Bloom, A. A.: Eval-

575   uating year-to-year anomalies in tropical wetland methane emissions using satellite CH4 observations, Remote Sensing of Environment, 211, 261–275, https://doi.org/https://doi.org/10.1016/j.rse.2018.02.011, 2018.

Parker, R. J., Wilson, C., Bloom, A. A., Comyn-Platt, E., Hayman, G., McNorton, J., Boesch, H., and Chipperfield, M. P.: Exploring constraints on a wetland methane emission ensemble (WetCHARTs) using GOSAT observations, Biogeosciences, 17, https://doi.org/10.5194/bg-17-5669-2020, publisher: Copernicus GmbH, 2020.

580   Patra, P. K., Houweling, S., Krol, M., Bousquet, P., Belikov, D., Bergmann, D., Bian, H., Cameron-Smith, P., Chipperfield, M. P., Corbin, K., Fortems-Cheiney, A., Fraser, A., Gloor, E., Hess, P., Ito, A., Kawa, S. R., Law, R. M., Loh, Z., Maksyutov, S., Meng, L., Palmer, P. I., Prinn, R. G., Rigby, M., Saito, R., and Wilson, C.: TransCom model simulations of CH_4 and related species: linking transport, surface flux and chemical loss with CH_4 variability in the troposphere and lower stratosphere, Atmospheric Chemistry and Physics, 11, 12 813–12 837, https://doi.org/10.5194/acp-11-12813-2011, 2011.

585   Patra, P. K., Krol, M. C., Prinn, R. G., Takigawa, M., Mühle, J., Montzka, S. A., Lal, S., Yamashita, Y., Naus, S., Chandra, N., Weiss, R. F., Krummel, P. B., Fraser, P. J., O'Doherty, S., and Elkins, J. W.: Methyl Chloroform Continues to Constrain the Hydroxyl (OH) Variability in the Troposphere, Journal of Geophysical Research: Atmospheres, 126, e2020JD033 862, https://doi.org/10.1029/2020JD033862, 2021.

Peng, S., Piao, S., Bousquet, P., Ciais, P., Li, B., Lin, X., Tao, S., Wang, Z., Zhang, Y., and Zhou, F.: Inventory of anthropogenic methane emissions in mainland China from 1980 to 2010, Atmospheric Chemistry and Physics, 16, https://doi.org/10.5194/acp-16-14545-2016,

590   2016.

Pickers, P. A. and Manning, A. C.: Investigating bias in the application of curve fitting programs to atmospheric time series, Atmospheric Measurement Techniques, 8, 1469–1489, https://doi.org/10.5194/amt-8-1469-2015, 2015.

Pickett-Heaps, C. A., Jacob, D. J., Wecht, K. J., Kort, E. A., Wofsy, S. C., Diskin, G. S., Worthy, D. E. J., Kaplan, J. O., Bey, I., and Drevet, J.: Magnitude and seasonality of wetland methane emissions from the Hudson Bay Lowlands (Canada), Atmospheric Chemistry and Physics,

595   11, 3773–3779, https://doi.org/10.5194/acp-11-3773-2011, 2011.

Prinn, R. G., Weiss, R. F., Arduini, J., Arnold, T., DeWitt, H. L., Fraser, P. J., Ganesan, A. L., Gasore, J., Harth, C. M., Hermansen, O., Kim, J., Krummel, P. B., Li, S., Loh, Z. M., Lunder, C. R., Maione, M., Manning, A. J., Miller, B. R., Mitrevski, B., Mühle, J., O'Doherty, S., Park, S., Reimann, S., Rigby, M., Saito, T., Salameh, P. K., Schmidt, R., Simmonds, P. G., Steele, L. P., Vollmer, M. K., Wang, R. H., Yao, B., Yokouchi, Y., Young, D., and Zhou, L.: History of chemically and radiatively important atmospheric gases from the Advanced

600   Global Atmospheric Gases Experiment (AGAGE), Earth System Science Data, 10, 985–1018, https://doi.org/https://doi.org/10.5194/essd-10-985-2018., 2018.

Randerson, J., Van Der Werf, G., Giglio, L., Collatz, G., and Kasibhatla, P.: Global Fire Emissions Database, Version 4.1 (GFEDv4), https://doi.org/10.3334/ORNLDAAC/1293, 2017.

Rigby, M., Montzka, S. A., Prinn, R. G., White, J. W. C., Young, D., O'Doherty, S., Lunt, M. F., Ganesan, A. L., Manning, A. J., Sim-

605   monds, P. G., Salameh, P. K., Harth, C. M., Mühle, J., Weiss, R. F., Fraser, P. J., Steele, L. P., Krummel, P. B., McCulloch, A., and Park, S.: Role of atmospheric oxidation in recent methane growth, Proceedings of the National Academy of Sciences, 114, 5373–5377, https://doi.org/10.1073/pnas.1616426114, 2017.

Sasakawa, M., Shimoyama, K., Machida, T., Tsuda, N., Suto, H., Arshinov, M., Davydov, D., Fofonov, A., Krasnov, O., Saeki, T., Koyama, Y., and Maksyutov, S.: Continuous measurements of methane from a tower network over Siberia, https://doi.org/10.17595/20160901.004, reference Date: 2022/10/20, 2010.

Saunois, M., Stavert, A. R., Poulter, B., Bousquet, P., Canadell, J. G., Jackson, R. B., Raymond, P. A., Dlugokencky, E. J., Houweling, S., Patra, P. K., Ciais, P., Arora, V. K., Bastviken, D., Bergamaschi, P., Blake, D. R., Brailsford, G., Bruhwiler, L., Carlson, K. M., Carrol, M., Castaldi, S., Chandra, N., Crevoisier, C., Crill, P. M., Covey, K., Curry, C. L., Etiope, G., Frankenberg, C., Gedney, N., Hegglin, M. I., Hoglund-Isaksson, L., Hugelius, G., Ishizawa, M., Ito, A., Janssens-Maenhout, G., Jensen, K. M., Joos, F., Kleinen, T., Krummel, P. B., Langenfelds, R. L., Laruelle, G. G., Liu, L., Machida, T., Maksyutov, S., McDonald, K. C., McNorton, J., Miller, P. A., Melton, J. R., Morino, I., Müller, J., Murguia-Flores, F., Naik, V., Niwa, Y., Noce, S., O'Doherty, S., Parker, R. J., Peng, C., Peng, S., Peters, G. P., Prigent, C., Prinn, R., Ramonet, M., Regnier, P., Riley, W. J., Rosentreter, J. A., Segers, A., Simpson, I. J., Shi, H., Smith, S. J., Steele, L. P., Thornton, B. F., Tian, H., Tohjima, Y., Tubiello, F. N., Tsuruta, A., Viovy, N., Voulgarakis, A., Weber, T. S., van Weele, M., van der Werf, G. R., Weiss, R. F., Worthy, D., Wunch, D., Yin, Y., Yoshida, Y., Zhang, W., Zhang, Z., Zhao, Y., Zheng, B., Zhu, Q., Zhu, Q., and Zhuang, Q.: The Global Methane Budget 2000–2017, Earth System Science Data, 12, 1561–1623, https://doi.org/10.5194/essd-12-1561-2020, 2020.

Scarpelli, T. R., Jacob, D. J., Moran, M., Reuland, F., and Gordon, D.: A gridded inventory of Canada's anthropogenic methane emissions, Environmental Research Letters, 17, 014 007, https://doi.org/10.1088/1748-9326/ac40b1, publisher: IOP Publishing, 2021.

Spivakovsky, C. M., Logan, J. A., Montzka, S. A., Balkanski, Y. J., Foreman-Fowler, M., Jones, D. B. A., Horowitz, L. W., Fusco, A. C., Brenninkmeijer, C. A. M., Prather, M. J., Wofsy, S. C., and McElroy, M. B.: Three-dimensional climatological distribution of tropospheric OH: Update and evaluation, Journal of Geophysical Research: Atmospheres, 105, 8931–8980, https://doi.org/https://doi.org/10.1029/1999JD901006, 2000.

Stavert, A. R., Saunois, M., Canadell, J. G., Poulter, B., Jackson, R. B., Regnier, P., Lauerwald, R., Raymond, P. A., Allen, G. H., Patra, P. K., Bergamaschi, P., Bousquet, P., Chandra, N., Ciais, P., Gustafson, A., Ishizawa, M., Ito, A., Kleinen, T., Maksyutov, S., McNorton, J., Melton, J. R., Müller, J., Niwa, Y., Peng, S., Riley, W. J., Segers, A., Tian, H., Tsuruta, A., Yin, Y., Zhang, Z., Zheng, B., and Zhuang, Q.: Regional trends and drivers of the global methane budget, Global Change Biology, 28, https://doi.org/10.1111/gcb.15901, 2022.

Thoning, K. W., Tans, P. P., and Komhyr, W. D.: Atmospheric carbon dioxide at Mauna Loa Observatory: 2. Analysis of the NOAA GMCC data, 1974–1985, Journal of Geophysical Research: Atmospheres, 94, 8549–8565, https://doi.org/https://doi.org/10.1029/JD094iD06p08549, 1989.

Tohjima, Y., Machida, T., Utiyama, M., Katsumoto, M., Fujinuma, Y., and Maksyutov, S.: Analysis and presentation of in situ atmospheric methane measurements from Cape Ochi-ishi and Hateruma Island, Journal of Geophysical Research: Atmospheres, 107, ACH 8–1–ACH 8–11, https://doi.org/https://doi.org/10.1029/2001JD001003, 2002.

Turner, A. J., Frankenberg, C., Wennberg, P. O., and Jacob, D. J.: Ambiguity in the causes for decadal trends in atmospheric methane and hydroxyl, Proceedings of the National Academy of Sciences, 114, 5367–5372, https://doi.org/10.1073/pnas.1616020114, 2017.

van der Werf, G. R., Randerson, J. T., Giglio, L., van Leeuwen, T. T., Chen, Y., Rogers, B. M., Mu, M., van Marle, M. J. E., Morton, D. C., Collatz, G. J., Yokelson, R. J., and Kasibhatla, P. S.: Global fire emissions estimates during 1997–2016, Earth System Science Data, 9, 697–720, https://doi.org/10.5194/essd-9-697-2017, 2017.

Weber, T., Wiseman, N. A., and Kock, A.: Global ocean methane emissions dominated by shallow coastal waters, Nature Communications, 10, 4584, https://doi.org/10.1038/s41467-019-12541-7, 2019.

645   Wilson, C., Chipperfield, M. P., Gloor, M., and Chevallier, F.: Development of a variational flux inversion system (INVICAT v1.0) using the
      TOMCAT chemical transport model, Geoscientific Model Development, 7, 2485–2500, https://doi.org/10.5194/gmd-7-2485-2014, 2014.

Wilson, C., Gloor, M., Gatti, L. V., Miller, J. B., Monks, S. A., McNorton, J., Bloom, A. A., Basso, L. S., and Chipperfield, M. P.: Contribution
      of regional sources to atmospheric methane over the Amazon Basin in 2010 and 2011, Global Biogeochemical Cycles, 30, 400–420,
      https://doi.org/https://doi.org/10.1002/2015GB005300, 2016.

650   Wilson, C., Chipperfield, M. P., Gloor, M., Parker, R. J., Boesch, H., McNorton, J., Gatti, L. V., Miller, J. B., Basso, L. S., and Monks,
      S. A.: Large and increasing methane emissions from eastern Amazonia derived from satellite data, 2010–2018, Atmospheric Chemistry
      and Physics, 21, 10 643–10 669, https://doi.org/10.5194/acp-21-10643-2021, 2021.

Zhao, Y., Saunois, M., Bousquet, P., Lin, X., Berchet, A., Hegglin, M. I., Canadell, J. G., Jackson, R. B., Hauglustaine, D. A., Szopa, S.,
      Stavert, A. R., Abraham, N. L., Archibald, A. T., Bekki, S., Deushi, M., Jöckel, P., Josse, B., Kinnison, D., Kirner, O., Marécal, V.,

655   O'Connor, F. M., Plummer, D. A., Revell, L. E., Rozanov, E., Stenke, A., Strode, S., Tilmes, S., Dlugokencky, E. J., and Zheng, B.: Inter-
      model comparison of global hydroxyl radical (OH) distributions and their impact on atmospheric methane over the 2000-2016 period,
      Atmospheric Chemistry and Physics, 19, 13 701–13 723, https://doi.org/10.5194/acp-19-13701-2019, 2019.

Table 1. List of 22 NOAA Sites used in the analysis (Dlugokencky et al., 2021).

Site Name	Latitude (° North)	Longitude (° East)	Site Code
Alert, Canada	82.45	-62.50	ALT
Ny-Alesund, Svalbard	78.91	11.80	ZEP
Barrow, Alaska, USA	71.32	156.60	BRW
Storhofdi, Vestmannaeyjar, Iceland	63.40	-20.28	ICE
Mace Head, Ireland	53.32	-9.90	MHD
Ulaan Uul, Mongolia	44.45	111.09	UUM
Niwot Ridge, Colorado, USA	40.05	-105.63	NWR
Terceira Island, Azores	38.70	-27.35	AZR
Mt Waligaun, Peoples Republic of China	36.27	100.92	WLG
Tudor Hill, Bermuda	32.26	-64.87	BMW
Izana, Tenerife	28.30	-16.48	IZO
Sand Island, Midway	28.22	-177.37	MID
Mauna Loa, Hawaii, USA	19.53	-155.58	MLO
Cape Kumukahi, Hawaii, USA	19.52	-154.82	KUM
Mariana Islands, Guam	13.39	144.65	GMI
Ragged Point, Barbados	13.17	-59.43	RPB
Mahe Isalnd, Seychelles	-4.68	55.53	SEY
Ascension Island, UK	-7.97	-14.40	ASC
Tutuila, American Samoa	-14.25	-170.56	SMO
Palmer Station, Antarctica	-64.92	-64.00	PSA
Sywoa Station, Antarctica	-69.00	39.57	SYO
South Pole, Antarctica	-89.98	-24.80	SPO

Table 2. List of 18 regions and their region code for each tracer.

Region Code	Region Name
AUS	Australasia
CAFR	Central Africa
CAN	Canada
CHJA	China & Japan
EBRA	East Brazil
EUR	Europe
INBA	India & Bangladesh
ME	Middle East
NAFR	North Africa
NAM	North America
NASA	Non-Amazon South America
NBRA	North Brazil
NOA	North Oceans & Arctic
RUS	Russia
SAFR	South Africa
SBRA	South Brazil
SEA	South East Asia
SOA	South Oceans & Antarctica

Table 3. List of the difference TOMCAT simulations.

TOMCAT Simulation	Experiment
TOM_regional	Regional tagged tracer simulation
TOM_transport	Investigating changes in transport
TOM_one	Background sensitivity - One month decay rate
TOM_twelve	Background sensitivity - Twelve month decay rate

Table A1. A table comparing the results ΔSCA (ppb) of TOM_regional, TOM_transport, TOM_twelve and TOM_one simulations.

Tagged Tracers	TOM_regional	TOM_transport	TOM_twelve	TOM_one
Total (sum of all tracers)	-6.38	-2.09	-6.38	-6.38
Sum of Regions	3.54	0.23	3.43	-2.61
Background	-9.93	-2.32	-9.81	-3.74
Canada	-2.97	0.24	-2.91	-4.09
Middle East	-2.13	-0.22	-2.14	-0.95
Europe	-1.48	0.76	-1.5	1.43
Russia	2.71	-0.60	2.67	1.56
North America	2.46	-0.91	2.52	0.52